Physica E 142 (2022) 115298

Contents lists available at ScienceDirect

Physica E: Low-dimensional Systems and Nanostructures

journal homepage: www.elsevier.com/locate/physe

Atomistic growth model with edge diffusion for chiral carbon nanotubes

T.D. Oke [a,1], S.I.V. Hontinfinde [b,d,1], M. Karimou [a,c,1], F. Zounmenou [d,1], F. Hontinfinde [a,d,*,1]

[a] IMSP Dangbo, Université d'Abomey-Calavi, Benin
[b] ENSGMM, Université d'Abomey, Benin
[c] ENSGEP, Université d'Abomey, Benin
[d] D'épartement de Physique, FAST, Université d'Abomey-Calavi, Benin

ARTICLE INFO

Keywords:
Chiral carbon nanotube
5-vertex model
Exact growth kinetics
Monte Carlo simulations
Growth modes

ABSTRACT

We carried out exact finite-size analysis and numerical simulation within a kinetic 5-vertex model to study the growth dynamics of chiral carbon nanotubes. The model comprises carbon atoms deposition and migration at the nanotube edge considered as Markov processes and a generalized Glauber dynamics is assumed. The physical parameters considered are the supersaturation of the carbon fluid phase, the synthesis temperature and the nanotube chirality which is known to be fixed by the nucleated cap. In the model, we are interested by the elongation of the nucleus in a tube. We calculated the growth rate and edge defect densities. The growth modes of the tube have been singled out in the model parameters' space. It has been found that spiral growth by pre-existing steps displacements is present beyond 1D-nucleation and continuous growth. In particular we obtained that in suitable physical conditions, the growth rate increases proportionally with the chiral angle θ of the nanotube up to a critical value θ_c which depends on values of model parameters.

1. Introduction

Single-walled (SW) carbon nanotubes (CNT) attracted broad interest in the past decades. They have exceptional properties: high levels of thermal, electrical and fluidic conductivity, high melting point and strong covalent bonds between carbon atoms. This makes them suitable for a wide range of applications: displays, photonics, composites and multifunctional coating/films, energy storage, transistors, etc [1–6]. They are characterized by the chiral angle θ between the tube edge circumference and the zig-zag motif of carbon atoms. Depending on this chirality, their electronic structure can be metallic or semiconducting. Controlled growth is therefore essential for practical realizations of current and emerging SWCNT devices. Chirality is however difficult to control in growth experiments which often proceed via chemical vapor deposition (CVD) [7,8] using metal nanoparticles as catalysts. The technique consists for instance in passing a hydrocarbon vapor through a tube furnace where the catalyst, maintained at very high temperature, decomposes the hydrocarbon. The CNT then grows on the catalyst and is collected upon cooling the system to room temperature [9]. The atomistic mechanisms behind this growth phenomenon are still not very well specified despite the myriad of theoretical and experimental investigations performed in the field. Theoretically, several growth models with screw dislocations have been investigated [10–12]. Some of them revealed that the growth velocity is proportional to the Burgers vector, i.e. to the chiral angle of the SWCNT.

Very recently, the growth kinetics of an achiral [13] SWCNT has been investigated by means of a kinetic 5-vertex model. In this model, carbon atoms adsorb from the gaseous phase at the CNT edge and stick where they land. No relaxation process by carbon atoms evaporation or migration at the CNT edge was considered. Exact results were provided for small-size versions of the model and larger sizes have been studied by kinetic Monte Carlo (KMC) simulations using the Bortz–Kalos–Lebowitz (BKL) update algorithm [14]. It was found that growth can proceed by 1D-nucleation or continuously at the nanotube edge. Kinks and steps densities at the growing nanotube edge have been calculated. Such a mapping of surface growth kinetics using vertex models has been performed in several previous works and revealed interesting growth properties [15–18]. In crystals growth, the growth of an exactly oriented and perfect crystal surface may occur by means of two-dimensional nucleation or a continuous mode [15]. The growth proceeds by incorporation of growth units into steps and kinks. Two incorporation modes are possible: direct atoms integration and atoms migration. For vicinal crystal surfaces, pre-existing steps may induce a step-flow mode.

In this work, we assume that a CNT of a certain chiral type is nucleated with axial screw dislocations. We then study the accretion

* Corresponding author.
E-mail address: fhontinfinde@yahoo.fr (F. Hontinfinde).
[1] All authors equally contribute to the present work in the calculations and in the manuscript writing process.

https://doi.org/10.1016/j.physe.2022.115298
Received 17 February 2022; Received in revised form 24 March 2022; Accepted 4 May 2022
Available online 17 May 2022

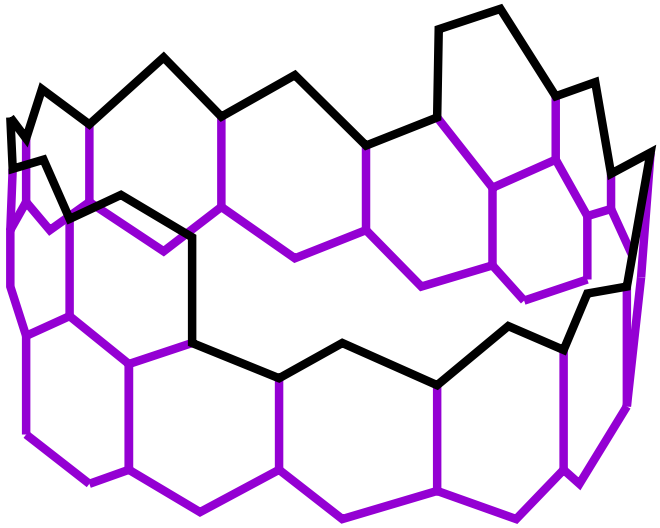

Fig. 1. A schematic view of the top profile of a single-walled carbon nanotube of size $L = 26$ with an axial dislocation with two monoatomic height steps. The CNT edge is illustrated with a black full line. This is an open-end model of the CNT used to feature the CNT elongation phenomenon after the nanotube nucleation on the catalyst particle where the chirality is selected. Carbon atoms are then assumed to flow from the catalyst to the nanotube edge with a well-determined flux that depends on the synthesis temperature and other factors (see text).

process of carbon atoms into the tube edge by introducing in the previous 5-vertex model [13], carbon atoms migration at the CNT edge. This extension makes the model more realistic from crystal growth processes point of view. We solve the model exactly for small system sizes and by numerical simulations for larger ones. We calculate the nanotube elongation rate, its edge defects densities and specify the different growth modes of the nanotube edge. We show that the chiral index of the CNT plays a crucial role in its growth kinetics in the presence of carbon atoms diffusion.

The paper is organized as follows. In Section 2, the kinetic 5-vertex model with edge diffusion is introduced and computational details are presented. Section 3 briefly describes the numerical simulation method. Section 4 is devoted to results and discussion. The last section contains concluding remarks.

2. Kinetic 5-vertex model for SWCNT growth

The chiral SWCNT edge shown in Fig. 1 (black full line) has two monoatomic height steps that result from an axial screw dislocation. This edge can be mapped onto a 5-vertex model [13]. The line representation of the 8-vertex model that comprises these relevant 5 vertices is depicted in Fig. 2. An illustration of the mapping is shown in Fig. 3 for a system of size $L = 26$ class (2) (hereafter referred to as the system (26,2)). It is noteworthy that according to the dislocation theory of Ding et al. [10], any chiral tube with conventional indices (n,m) can be viewed as a basic zig-zag but with a running through center-hollow screw dislocation of a Burgers vector **b**. This means that for a given chiral nanotube, one just needs to consider as sample, the zig-zag edge and then create screw dislocation defects corresponding to these indices as explained in this reference and apply the present mapping onto the 5-vertex model.

The SWCNT chiral class is defined in the model by the number $c = N_7 - N_8$, where N_7/N_8 denotes the number of vertex of type 7/8 used in the mapping. Classes with opposite numbers c display the same growth kinetics due to reflection symmetry. Since only topmost atoms of the CNT edge are assumed to belong to it, vertices 1, 2 and 3 are useless in the mapping of the edge kinetics. Vertex energies are defined assuming that the achiral CNT with zigzag edge mapped with only vertices 5 and 6 ($c = 0$) should have zero energy. Thus, other vertices appearing during the CNT edge fluctuations would be assigned the same non-zero energy ϵ. One gets: $\epsilon_5 = \epsilon_6 = 0$; $\epsilon_4 = \epsilon_7 = \epsilon_8 = \epsilon$. The exact solution of this kinetic 5-vertex model uses a technique described in some previous works [13,15–18]. The 5-vertex configurations of a given CNT system are ranged into time-conserved classes divided into non-conserved subclasses where configurations are equivalent by translations. The number of subclasses rapidly increases with the system size. For $L = 14$ class (4)/(8), 1858/162 subclasses are got.

During the SWCNT growth, an edge 5-vertex configuration runs from one subclass to another within the same class. This enables to define a transition matrix between subclasses. For $L = 14$, class (4), a 1858×1858 transition matrix is obtained.

Let us consider the CNT system (6,2). Its 5-vertex configurations belong to 9 subclasses S_i, i=1,9, which witness configurations are illustrated in Fig. 4.

A deposition site at the interface is characterized by a 5-vertex subconfiguration formed by three vertices that we termed growth kink subconfigurations (growth active sites). A number of 8 growth kink subconfigurations are found in the model:

$$K_1 = 856, \quad K_2 = 656, \quad K_3 = 857, \quad K_4 = 657,$$
$$K_5 = 464, \quad K_6 = 768, \quad K_7 = 764, \quad K_8 = 468.$$

A diffusion site at the interface is characterized by a 5-vertex subconfiguration formed by four vertices that we termed diffusion kinks. We also have 8 different types of these kinks:

$$\overline{K}_1 = 4656, \quad \overline{K}_2 = 4657, \quad \overline{K}_3 = 4764, \quad \overline{K}_4 = 4768,$$
$$\overline{K}_5 = 6564, \quad \overline{K}_6 = 8564, \quad \overline{K}_7 = 4684, \quad \overline{K}_8 = 7684.$$

The four former kinks $\overline{K}$ are diffusion kinks to the right while the latters which are the vertical mirror images of the formers are diffusion kinks to the left. The change in the 5-vertex energy ΔE associated are, in units of ϵ, 0,0,-2,-3,0,0,-2,-3 respectively. It could be remarked that in the model, the CNT edge relaxes through these carbon atoms migration events by either conserving or lowering its energy.

The dynamics is introduced in the model by carbon atom attachments (e.g. process (a) in Fig. 4) and migrations (e.g. process (b) in Fig. 4) at the SWCNT edge. The CNT growth is the product of competing processes occurring at different time scales: disordering through carbon atoms deposition at the CNT edge at rate C and ordering through carbon adatoms migration at a hopping rate given by the conventional Arrhenius ansatz: $D = D_0 exp(-\beta E_0)$ where D_0 denotes the attempt frequency and E_0 the hopping energy barrier, $\beta = 1/k_B T$ is the inverse synthesis temperature, k_B the Boltzmann constant set to 1 in the following.

Rates of deposition processes follow the generalized Glauber dynamics expressed in the form [13]:

$$C = \frac{exp(\beta\Delta\mu)}{1 + exp(\beta\Delta E)}, \tag{2.1}$$

where $\Delta\mu$ (so-called driving force) is the difference in chemical potential between the solid tube phase and the carbon gaseous phase, and ΔE the change in the 5-vertex energy of the system during the considered attachment process. Denoting by $u = \exp(\beta\Delta\mu)$ and $v = \exp(\epsilon/T)$, transition rates C_i (i=1,8) associated to previous growth kinks are respectively:

$$C_1 = \frac{u}{1+v}, C_2 = C_3 = C_4 = C_1, C_5 = \frac{1}{2}u,$$
$$C_6 = \frac{u}{1+v^{-2}}, C_7 = \frac{u}{1+v^{-1}}, C_8 = C_7$$

For the carbon atoms migration, events are also considered as Markov processes which rates are assumed to be in the same form as the deposition rates:

$$D = D_0 \frac{exp(-\beta E_0)}{1 + exp(\beta\Delta E)}, \tag{2.2}$$

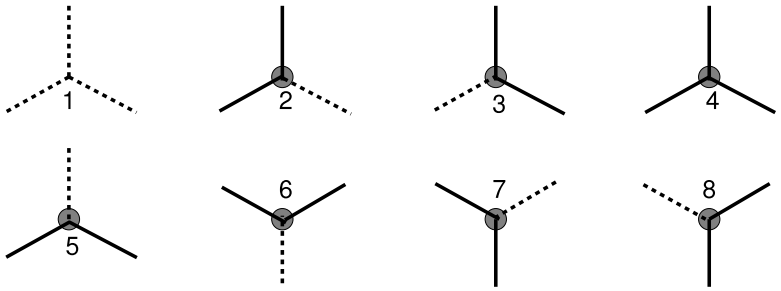

Fig. 2. Schematic line representation of the 8-vertex model.

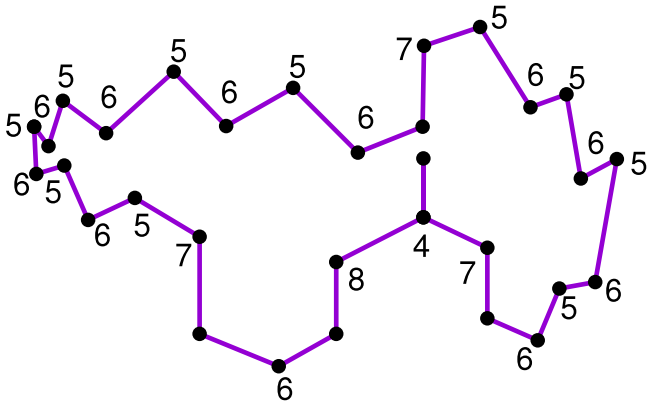

Fig. 3. Mapping of a SWCNT growing edge of length $L = 30$ and class (2) onto the 5-vertex model. In the mapping, full lines of the vertices are considered and dashed lines are omitted.

where the attempted frequency D_0 is assumed to depend weekly on the temperature. In the following, it will be taken either as a constant (see [19–21] and references therein) set to 1 (model M_1) or proportional to the typical vibration frequency of an isolated carbon adatom on the CNT edge (model M_2): $D_0 \simeq kT/h$ [22] where h is the Planck constant (hereafter set to 1); E_0 is the activation energy that is assumed to be a constant set to ϵ for all diffusion processes. In this formulation, it is evident that the diffusion process is also activated by the change of the environment of the diffusion kink during the diffusive motion. This is measured by ΔE. Associated rates are summarized as follows:

$$D_1 = D_2 = D_5 = D_6 = D_0\frac{1}{2v}, D_3 = D_7 = D_0\frac{1}{v+v^{-1}},$$
$$D_4 = D_8 = D_0\frac{1}{v+v^{-2}}$$

The case of pure deposition model will be referred to as model M_0. This corresponds to the diffusion model with an infinite energy barrier. The relation (2.1) (see Ref. [13,23]) is the product of the carbon atomic flux given by $exp(\Delta\mu/T)$ and the conventional Glauber transition probabilities $1/(1+exp(\Delta E/T))$ [24] often used in the simulation of the Ising model [25,26]. Relation (2.2) is got in the same way.

In equilibrium as in dynamics, a time-dependent statistical weight $P_m(t)$ is associated with each subclass. The $P_m(t)$ evolves in the course of the time following the kinetic equation:

$$\frac{dP_m(t)}{dt} = -\sum_a (C_a p_m^a + D_a q_m^a)P_m(t) + \sum_{a,n}(C_a M_{mn}^a + D_a N_{mn}^a)P_n(t) \qquad (2.3)$$

where p_m^a/q_m^a is the multiplicity of growth/diffusion kinks of type a in the mth subclass; C_a/D_a denotes the sticking/diffusion rate at the growth/diffusion kink of type a; M_{mn}^a/N_{mn}^a is the number of times that a configuration of the mth subclass is obtained from a configuration of the nth subclass by evolution (deposition/migration) of the kink of type a.

The previous equation can be written in the form:

$$\frac{d[P_m(t)]}{dt} = [M].[P_m(t)] \qquad (2.4)$$

where $[M]$ denotes the transition matrix between subclasses within the selected class. For $L = 6$, class (2), this matrix reads:

$$M = \begin{pmatrix} -C_{58} & C_2 & 0 & 0 & C_1 & 0 & 0 & 0 & 0 \\ 0 & -C_{21} & 0 & 0 & D_6 & C_6 & C_1 & 0 & 0 \\ 0 & 0 & -C_{87} & C_1 & 0 & 0 & 0 & 0 & 0 \\ C_8 & \}0 & 0 & -C_{18} & 0 & 0 & 0 & 2C_1 & 0 \\ 0 & D_1 & 2C_8 & 0 & -C_{186} & 0 & C_2 & 0 & 0 \\ 0 & 0 & 0 & 0 & 0 & -C_{64} & 0 & 0 & C_3 \\ 0 & 0 & D_7 & C_8 & 0 & D_4 & -C_{12} & 0 & C_6 \\ 0 & 0 & 0 & 0 & C_8 & 0 & 0 & -2C_1 & 0 \\ C_5 & 0 & 0 & 0 & 0 & 0 & 0 & 0 & -C_{36} \end{pmatrix} \qquad (2.5)$$

with:

$C_{58} = C_5 + C_8$; $C_{21} = C_2 + D_1$; $C_{87} = 2C_8 + D_7$; $C_{18} = C_1 + C_8$; $C_{186} = C_1 + C_8 + D_6$; $C_{64} = C_6 + D_4$; $C_{12} = C_1 + C_2$; $C_{36} = C_3 + C_6$.

The time-dependent growth rate per site $G(t)$ is defined by:

$$G(t) = L^{-1}\sum_{a,m} C_a p_m^a P_m(t), \qquad (2.6)$$

where p_m^a denotes the multiplicity of kink of type a in the mth subclass.

In the steady growth regime, $\frac{d[P_m(\infty)]}{dt} = [0]$. In this case, for $L = 6$, class (2) the subclass weights can be analytically evaluated:

$$P_1(\infty) = \frac{C_3 + C_6}{C_5}P_9(\infty),$$
$$P_2(\infty) = \frac{b_1b_6 + b_3b_5}{b_2b_6 + b_3b_4}P_9(\infty),$$
$$P_3(\infty) = [\frac{C_1C_8(C_3 + C_6)}{C_5(2C_8 + D_7)(C_1 + C_8)} + \frac{C_1C_8(b_1b_4 - b_2b_5)}{(C_1 + C_8)((2C_8 + D_7))(b_2b_6 + b_3b_5)}]P_9(\infty),$$
$$P_4(\infty) = [\frac{C_8(C_3 + C_6)}{C_5(C_1 + C_8)} + \frac{C_8(b_1b_4 - b_2b_5)}{(C_1 + C_8)(b_2b_6 + b_3b_5)}]P_9(\infty),$$
$$P_5(\infty) = \frac{b_1b_4 - b_2b_5}{b_2b_6 + b_3b_5}P_9(\infty),$$
$$P_6(\infty) = \frac{C_3}{C_6 + D_4}P_9(\infty),$$
$$P_7(\infty) = [\frac{C_8C_8(C_3 + C_6)}{(C_1 + C_2)C_5(C_1 + C_8)} + \frac{C_8C_8(b_1b_4 - b_2b_5)}{(C_1 + C_2)(C_1 + C_8)(b_2b_6 + b_3b_5)} + \frac{C_6}{(C_1 + C_2)} + X1 + X_2]P_9(\infty),$$
$$P_8(\infty) = \frac{C_8(b_1b_4 - b_2b_5)}{2C_1(b_2b_6 + b_3b_5)}P_9(\infty),$$
$$b_1 = -\frac{(C_5 + C_8)(C_6 + C_3)}{C_5},$$

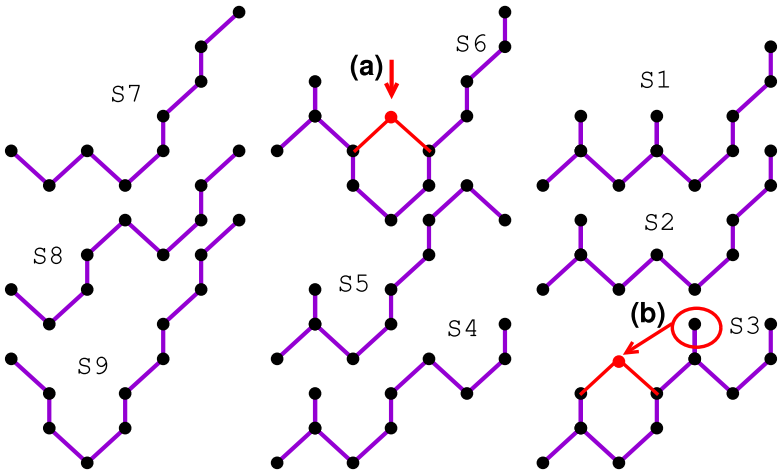

Fig. 4. Schematic representations of witness configurations of the 9 subclasses of the system (6,2). There is one carbon atom which is represented twice at both ends of each SWCNT edge due to periodic boundary conditions. One can see through these configurations that the system comprises dislocations. The witness configuration of S_8 shows two equidistant monoatomic height axial dislocation steps. Two processes are illustrated in the figure. Process (a) is a deposition event that leads the S_6 witness configuration into S_2. Process (b) is an interlayer diffusion event which leads the S_3 witness configuration into S_7. Changes that occur in the CNT edge morphology are indicated by red segments.

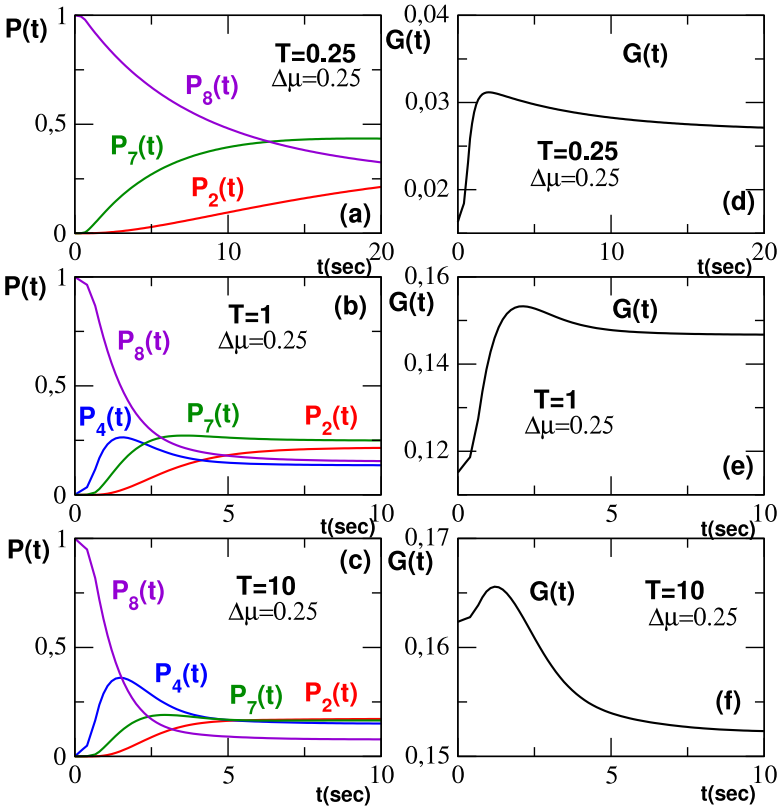

Fig. 5. Exact time-evolution of important subclass weights for the system (6,2) at three selected temperatures: $T = 0.25$ (a), $T = 1$ (b) and $T = 10$ (c) for $\Delta\mu = 0.25$. Using these results, $G(t)$ has been evaluated and found to level off at a constant in the long-time limit (panels d, e, f).

$$b_2 = C_2,$$
$$b_3 = C_1,$$
$$b_4 = C_2 + D_1,$$
$$b_5 = \frac{C_6C_3}{C_6 + D_4} + \frac{C_1C_8C_8(C_3 + C_6)}{C_5(C_1 + C_2)(C_1 + C_8)} + \frac{C_1C_6}{C_1 + C_2} + \frac{C_1D_4C_3}{(C_1 + C_2)(C_6 + D_4)} + X_0,$$
$$b_6 = -\frac{C_1C_8C_8}{(C_1 + C_2)(C_1 + C_8)} + \frac{C_1C_1C_8D_7}{(C_1 + C_2)(C_1 + C_8)(2C_8 + D_7)} + D_6,$$
$$X_0 = \frac{D_7C_1C_1C_8(C_3 + C_6)}{C_5(C_1 + C_2)(2C_8 + D_7)(C_1 + C_8)},$$
$$X_1 = \frac{D_7}{(C_1 + C_2)}\left[\frac{C_1C_8(C_3 + C_6)}{C_5(2C_8 + D_7)(C_1 + C_8)} + \frac{C_1C_8(b_1b_4 - b_2b_5)}{(C_1 + C_8)((2C_8 + D_7))(b_2b_6 + b_3b_5)}\right],$$

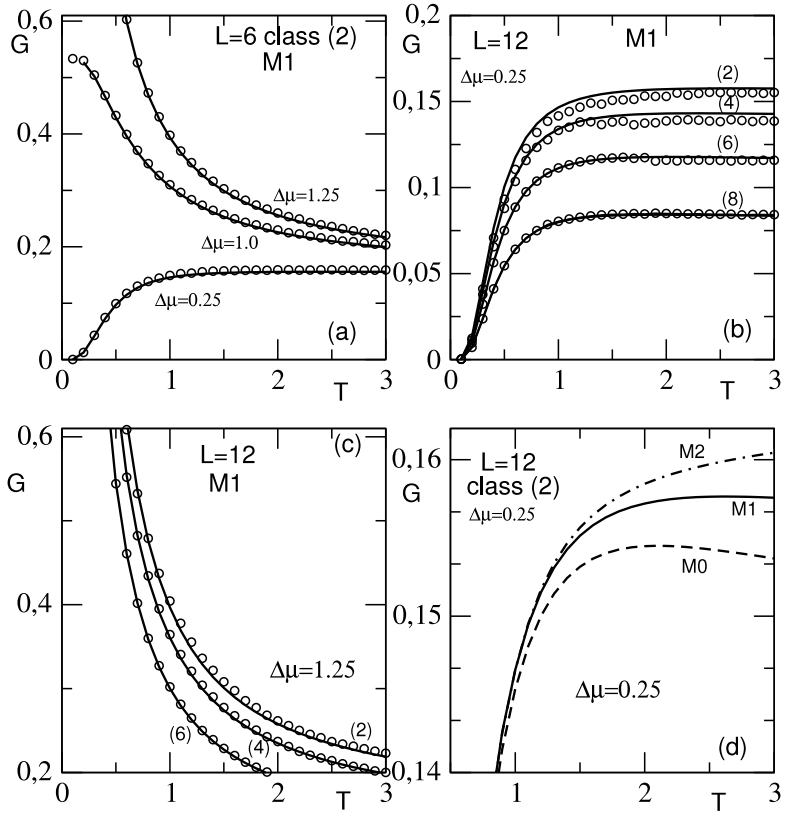

Fig. 6. Exact (lines) and simulated (signs) steady growth rates G versus synthesis temperature T are illustrated for several values of $\Delta\mu$ and system classes. In panel (a), the system (6,2) is considered and numbers written on the curves are selected values of the driving force $\Delta\mu$. It is evident that at a given temperature, the growth rate G is an increasing function of $\Delta\mu$. For small values of $\Delta\mu$, G has an initial exponential behavior which is according to the Becker–Doering law (see text), taken as the domain of layer-by-layer growth mode. In panel (b), results are provided for systems (12,2), (12,4), (12,6), (12,8). In panel (d), exact results for three models, M_0, M_1, M_2 are depicted. For M_1 and M_2 no decreasing part is found at high temperature contrarily to what occurs for model M_0. An impressive agreement is observed between exact and simulation results in panels (a), (b) and (c). In panel (d), it is observed that the nanotube elongation rate is enhanced at high temperature by carbon atoms diffusion processes.

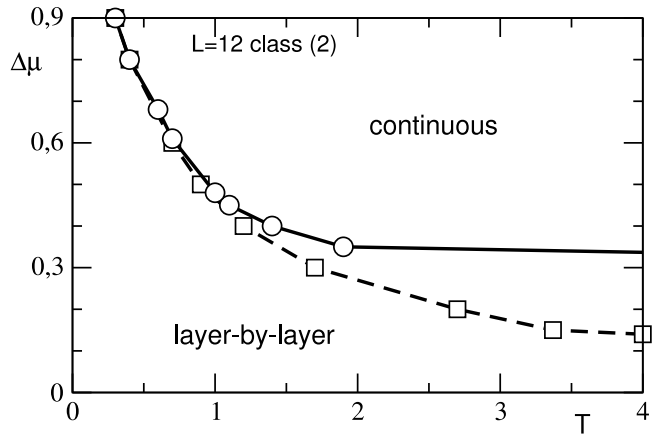

Fig. 7. Exact growth phase diagrams for the system (12,2) illustrated for models M0 (open squares: only deposition events) and M2 (circles: deposition with migration events). Above transition lines, the growing CNT edge should be "rough". Below, the edge may have less defects and grow while remaining fairly flat. At high temperature, carbon atoms migration events due play a smoothening effect and an expansion is observed for the layer-by-layer domain.

$$X_2 = \frac{D_4 C_3}{(C_1 + C_2)(C_6 + D_4)}$$

Setting $P_9(\infty) = 1$, one gets

$$G = \frac{1}{6}(C_5 + C_8)\tilde{P}_1 + (C_2)\tilde{P}_2 + (2C_8)\tilde{P}_3 + (C_1 + C_8)\tilde{P}_4 + \tilde{X_0} \tag{2.7}$$

with

$$\tilde{X_0} = (C_1 + C_8)\tilde{P}_5 + (C_6)\tilde{P}_6 + (C_1 + C_2)\tilde{P}_7 + 2C_1\tilde{P}_8 + (C_3 + C_6)\tilde{P}_9,$$

where $\tilde{P}_i$, $i = 1, \ldots, 9$ are normalized subclass weights.

Curves related to this exact growth rate are depicted with full lines in Fig. 6a. This exact analytical calculation which results coincide with those from our numerical code could be performed only for a very small systems. For relatively larger ones, the transition matrix is constructed by means of the code which has also its limitations due to the need of larger computer memory and computing time. Much larger samples are treated with Monte Carlo simulations.

3. Numerical simulations

The kinetic Monte Carlo simulations with the Bortz, Kalos Lebowitz (BKL) algorithm is adopted [14–22]. In the BKL scheme, a move is performed at each step according to its a priory probability. For a CNT edge 5-vertex configuration (C) obtained at a given stage of the growth with Ω possible processes (atoms deposition and diffusion) with transition rates T_n, $n = 1, \Omega$, the total evolution rate R of (C) is the sum of transition rates of possible events on (C). The real life-time of (C) is given by:

$$\tau = -Log(r)/R \tag{3.1}$$

where r is a random number generated between 0 and 1. Another random number r_1 is selected and a random rate $Q = r_1 \times R$ is evaluated. By summing rates of updated processes of configuration (C), the first process such that the condition

$$\sum_{n=1} T_n \geq Q \tag{3.2}$$

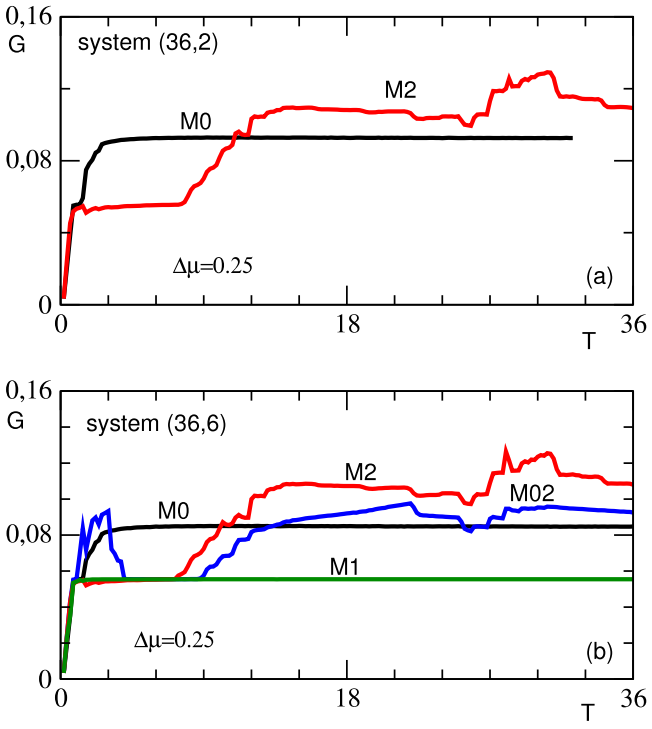

Fig. 8. Simulated growth rates versus temperature T for models M_0, M_1, M_2 and M_{02} (see text). Model M_{02} is model M_2 minus interlayer diffusion. Systems (36,2) and (36,6) are considered. The driving force is set to $\Delta\mu = 0.25$. It results that the growth velocity is enhanced at high synthesis temperature in the presence of carbon atoms migration processes and the interlayer diffusion mechanism is playing a major role.

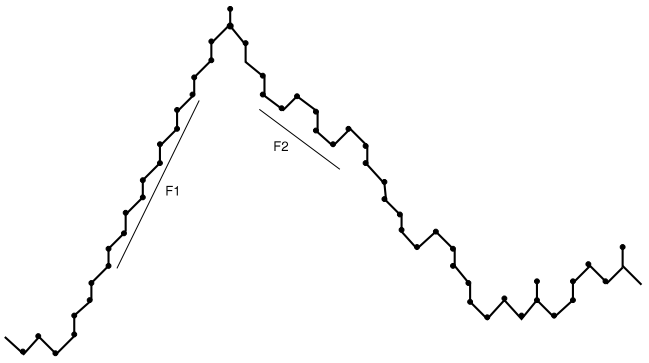

Fig. 9. Snapshot of a growing edge of the CNT system (36,2) at $T = 30$, $\Delta\mu = 0.25$. Two nanofacets F_1 and F_2 (armchair) are visible. The circular edge presents a big mound with large inclinations. This picture indicates a kind of unstable growth which should arise from the uphill atomic current at the nanotube edge (see Ref. [27]).

holds is realized. Then possible processes of the new 5-vertex configuration are updated and the total evolution rate recalculated. After a sufficient simulation time period t where g new configurations have been generated, values of physical quantities are estimated by a time-averaging procedure. Thus, the growth rate G at the steady state is evaluated as follows:

$$G = t^{-1}L^{-1}\sum_{n=1}^{g}\tau(C_n)R(C_n) \tag{3.3}$$

In the same way, an edge defect density of type k could be calculated as an average other different configuration contributions:

$$d_k = t^{-1}L^{-1}\sum_{n=1}^{g}\tau(C_n)N_k(C_n) \tag{3.4}$$

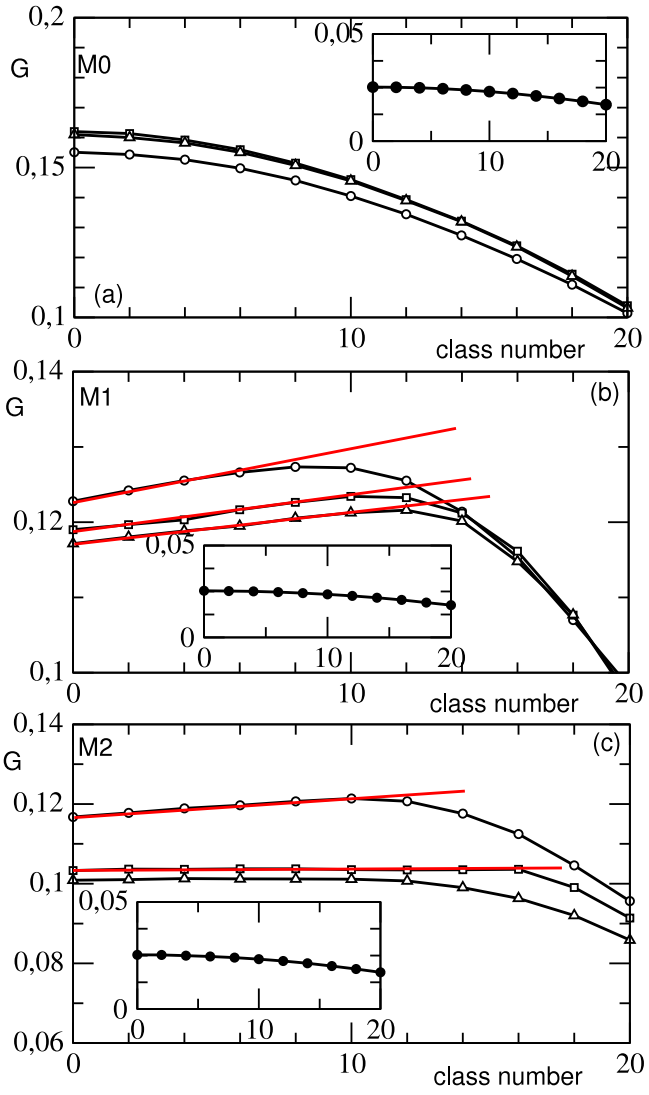

Fig. 10. KMC simulated growth rates as functions of parameter c for $L = 30$ at four temperatures: $T = 0.25$ (full circles, inset curves); $T = 1.25$ (open circles); $T = 2.25$ (open squares); $T = 3.25$ (open triangles). One sees that for three diffusion models, the growth velocity can increase quasi-linearly or be constant with increasing chiral index up to some critical value that depends on the diffusion model and the temperature. These results are consistent with findings by Ding et al. from Ref. [10]. Red lines indicate the linear profile of the curves. Following Ref. [10], one can predict that due to the existence of such correlation (increase of the elongation rate with chirality), the abundance of chiral nanotubes in experiments should be proportional to their chiral angles.

where $N_k(C_n)$ is the number of defect of type k in configuration (C_n).

By analyzing growth rates or defect densities, one is able to guess some insight into the role of different types of kink or defect in the SWCNT edge kinetics and growth modes.

4. Results and discussion

The temperature T, the driving force $\Delta\mu$ which is related to the pressure of the gaseous carbon phase and all energies are expressed in units of ϵ. In Fig. 5, the time-evolution of some important subclass weights are illustrated for three selected temperatures at $\Delta\mu = 0.25$ as well as the CNT elongation rate $G(t)$. In all panels, growth starts from an edge configuration belonging to S_8 with a local armchair nanofacet (see facet F_2 in Fig. 9). However, the long-time limit edge configurations are found to mainly belong to S_2 and S_7. Configurations of these subclasses

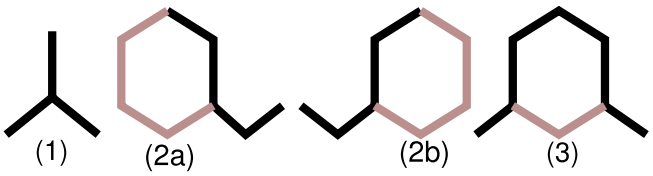

Fig. 11. Schematic representation of some defects at the chiral tube edge during growth: (2a) and (2b) are traditional steps with a kink site each; (3) is an hexagon at the tube edge with two opposite steps which arises from carbon dimers formation; (1) symbolizes an adatom on a zig-zag edge. Monoatomic steps at the edge comprise pre-existing steps due to screw dislocations and new steps created on terraces.

have two correlated vertex 8. This means that the steady state edge configuration is also faceted (see facet F_1 in Fig. 9) with less diffusion kinks. At $T = 1$, similar results are obtained in the steady state. On the contrary, at $T = 10$, configurations of S_4 become also relevant and the steady state edge is composed of facets F_1 and F_2.

In Fig. 6 (panels a,b and c), results are related to the diffusion model M_1. In Fig. 6a, exact (full lines) and KMC (signs) CNT elongation rates are compared for three selected values of $\Delta\mu$. An impressive accuracy is got, in particular when the involved transition matrix is not very large. It is observed that the growth rate for small values of $\Delta\mu$ is very small at low temperature. Then, it increases with the temperature, passes through a maximum and decreases. Above $\Delta\mu = 1$, G is a monotonically decreasing function of T. The initial exponential behavior of G is useful in extracting the step free energy per unit length by means of Arrhenius plots when one invokes the Becker–Doering law of crystal growth by 2D-nucleation mechanism [28–30]. Following this law, one can speculate that in this range of exponential growth, growth proceeds layer-by-layer with the SWCNT edge remaining fairly flat. An energy barrier for the growth can also be extracted from this trend. Beyond, G decreases exponentially, following the Wilson–Frenkel law [31,32] (panel c). Hence a continuous growth mode is obtained. In this regime, the change of the surface 5-vertex energy in the deposition process becomes irrelevant. The temperature associated to the maximum growth rate could be roughly taken as the transition temperature between these two growth modes. This has been done in several previous works [13,16,17] with kinetic vertex models for crystals growth. Hence, the presence of carbon atoms migrations at the SWCNT rim does not alterate this layer growth mode. On the contrary, as we will show later, it amplifies it in some model parameters' ranges. In Fig. 6b, G is plotted against T for selected values of the chiral index given by the parameter c for an edge of circular length $L = 12$. G is a decreasing function of the chiral index (see also panel c). In Fig. 6d, exact growth rates are illustrated for three models M_1, M_2 and M_0. It is observed that the elongation rate increases in the presence of carbon atoms migration in the range of temperature investigated. This may be a key result of the present model for CNT growth: the diffusion process speeds up the CNT elongation process. The panel (d) bears another important finding. It is evidenced that the maximum growth rate is obtained for models M_1 and M_0 at the same temperature which is lower than that of model M_2. This means that the region of layer-by-layer growth mode related to the temperature associated to the maximum growth rate expands when interface relaxation events are effective in the model M_2. One should mainly assist to a sequential accretion of diffusing carbon atoms along the spiral ladder of the CNT rim [33] in addition to the 1D-nucleation mechanism previously indicated by the exponential increasing part of G. An exact growth phase diagram is depicted in Fig. 7 for the system (12,2) and the layer-by-layer growth domain expands at high temperature as a consequence of carbon atoms migration. Calculations indicated that increasing the driving force $\Delta\mu$ or the atomic flux reduces atoms migration processes since both events compete in the model. We check that previously reported results bear some finite-size effects. Indeed, on larger systems, a different growth

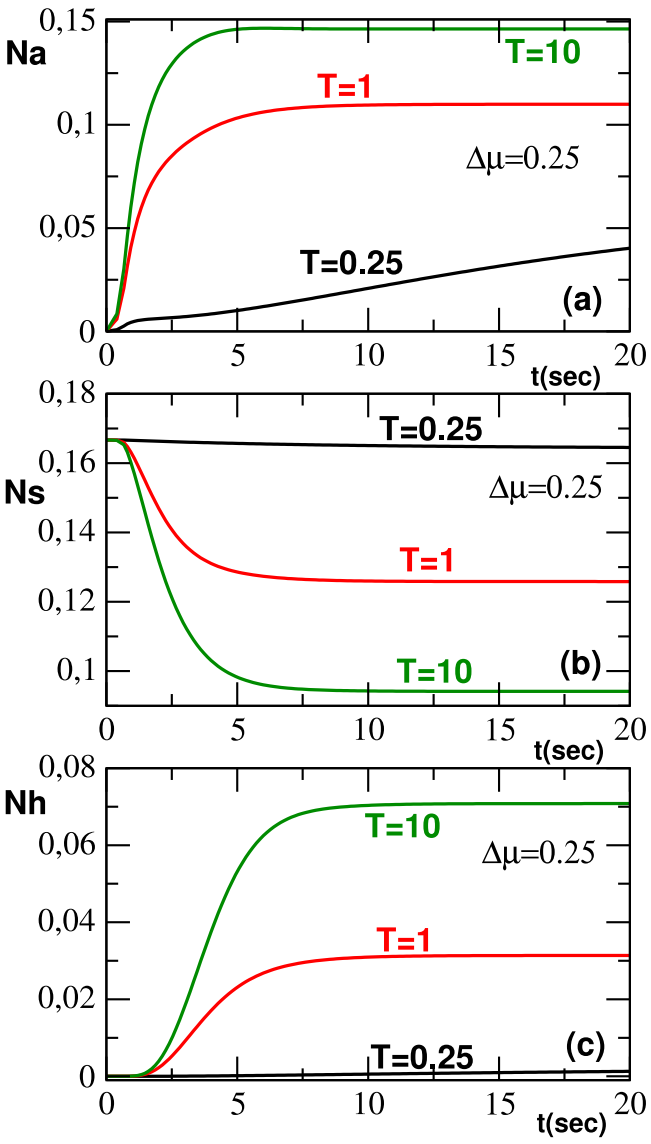

Fig. 12. Adatom (Na), Step (Ns) and Hexagon (Nh) densities as functions of the real growth time for the system (6,2). In the calculations, growth starts from an initial configuration of the system belonging to S_8. Na increases with the temperature and tends to saturate in the long-time limit. Nh decreases with increasing temperature. Ns is constant at $T = 0.25$ while $Nh = 0$. The latter suggests an early-time step propagation mode with almost no hexagon nucleation events on the CNT edge.

picture arises. In Fig. 8, compared simulated growth rates G are illustrated for different models for systems (36,2) and (36,6). Reported growth rates have been averaged other 2.10^3 independent runs with 3.10^3 Monte Carlo steps per site each. The indicated model M_{02} refers to model M_2 where interlayer diffusion (e.g. process b in Fig. 4) which plays a key edge smoothening effect in the growth is suppressed. In Fig. 8a, it is evidenced that at low temperature, no fundamental differences exist in the growth rates by models M_0 and M_2. This temperature range corresponds to deposition-dominated regime and carbon atoms migration processes are almost absent. One finds an intermediate temperature range where migration events do not speed up the growth process since curves by M_2 lays below that by M_0. This is somewhat strange due to the smoothening nature of diffusion processes often observed in crystal growth. Low values of G means that few growth sites are available. This situation can only occur if the CNT edge is strongly faceted with correlated vertices 7 or 8, which situation decreases the number of potential growth and diffusion kinks.

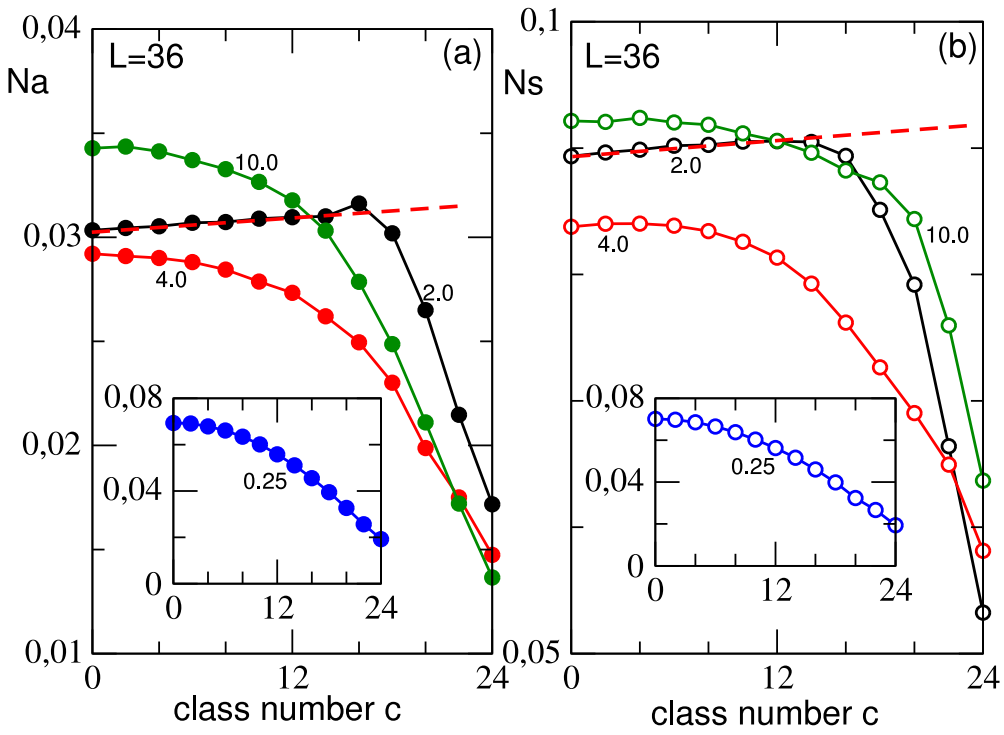

Fig. 13. KMC simulated adatom and step densities versus class number c at $\Delta\mu = 0.25$ for the system size $L = 36$. Selected temperatures are $T = 0.25$ (inset); 2.0; 4.0 and 10.0 written on the curves. The diffusion model M_2 is used for the simulations. At $T = 2$, a linear behavior of adatom and step densities with the chiral angle related to the class number parameter c is observed up to a critical value of c.

The situation changes with a further increase of the temperature. A snapshot of the linear view of the CNT edge in this region is given in Fig. 9 at $T = 30$. One can see a big mound with large inclinations to a quasi-flat valley. Some characteristic nanofacets (F_1 and F_2) are formed at the edge. The valley shows potential diffusion and growth kinks that could evolve to stabilize the growing edge. The evolution of these kinks induces an edge energy change of -3ϵ or -2ϵ. This speeds up the CNT elongation rate since most events consist in closing open hexagons.

In Fig. 8b, Model M_1 yields bad results at high temperature for the CNT edge growth rate since the latter is lower that in the case where diffusion is absent (Model M_0). Atomic diffusion in this model destabilizes the moving surface at high temperature. This means that model M_2 with the prefactor T is more reliable leading to a more stable growth. Comparing curves by M_{02}, M_2 to that by M_0, one remarks that the diffusion mechanism is playing a major role in the edge kinetics, in particular the interlayer diffusion. The suppression of the latter decreases the growth rate in some model parameters ranges.

In Fig. 10, the growth rates versus the parameter c related to the chiral index of the CNT are illustrated for three models M_0, M_1, M_2 at four temperatures: $T = 0.25$ (full circles) $T = 1.25$ (open circles), $T = 2.25$ (open squares), $T = 3.25$ (open triangles). The low-temperature growth refers to the deposition-dominated regime and diffusion processes are irrelevant as no fundamental changes occur in the growth rate for three models (see inset curves). This is consistent with the low-temperature observations in Fig. 8 and the three models are equivalent at $T = 0.25$. The high-temperature growth is associated to the diffusion-dominated regime. There, a landed carbon atom has enough time to reach a step before meeting another diffusing atom of before another one lands at a nearby growth site. Beyond $T = 0.25$, differences appear. In the absence of diffusion events the growth is a monotonically decreasing function of the edge parameter c with a quasi-parabolic shape (see inset curves). When the edge relaxes through atoms migration, a different picture is revealed at intermediate and high temperatures (see main curves). G increases with increasing values of c, passes through a maximum and then decreases for large values. These results obtained in the diffusion-dominated regime are quite similar to those previously reported in Ref. [27] on a single-step growth model with surface diffusion which led to a phase separation phenomenon.

From the above, one remarks that for low values of c in the diffusion-dominated regime, the growth rate shows a linear increasing behavior for both M_1 and M_2. This indicates that in this physical parameters range, the growth rate is proportional to the chiral angle of the CNT. In other ranges it should not happen. This is a crucial result of the present kinetic model for chiral CNT growth which is somewhat consistent with results previously reported by Ding et al. in Ref. [10]. This means that suitable choice of values of parameters are required to get this correlation. Therefore, it could not be observed in all CVD experiments. This statement is consistent with reports from Refs. [7,8,34,35].

Fig. 11 illustrates some CNT edge defects. Their densities during the growth can help in getting some insight into the growth kinetics, modes and morphology. A constant step density and hexagon density with small adatom density during the growth should result from pre-existing steps displacement (step-flow) mode. A low step density and a high adatom or hexagon density should characterize a rough growing edge. Faceted or unstable growing edge may be characterized by low density of adatoms, steps and hexagons. Following these features, one is able to interpret results from Fig. 12. At $T = 0.25$, the early-time growth mode is that of step propagation. At $T = 1.0$, hexagons are nucleated at the edge and a 1D-nucleation mechanism is expected. At $T = 10.0$, results indicate a rough growing edge.

In Fig. 13, the behaviors of the defect densities with varying class numbers c are illustrated on a system of circular size $L = 36$. N_a and N_h behave similarly at $T = 0.25$. At $T = 2$, both densities show an increase with c up to a critical value beyond which they decrease. One observes plateau values for N_s up to some critical values of c which depend on the temperature. Similar results have been reported in Ref. [27] for the adatom density as function of the system tilt. The simulations indicate that at $T = 2$, G, N_a and N_s evaluated in the steady

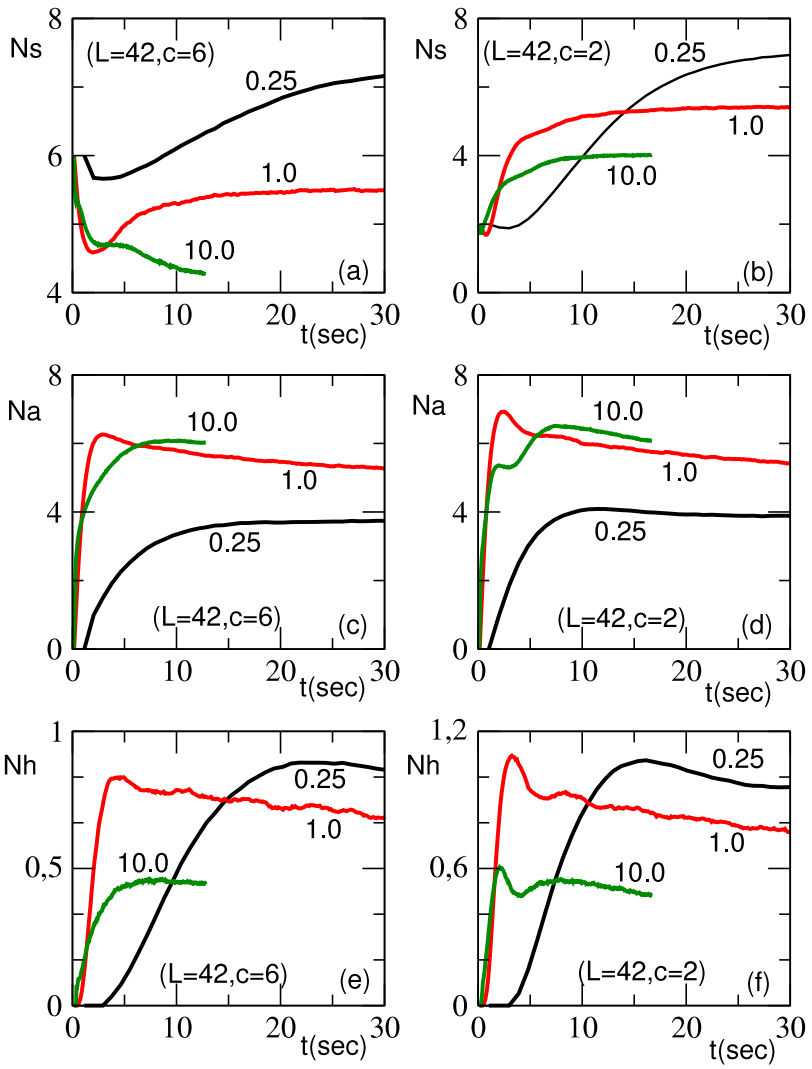

Fig. 14. Time-behavior of the adatom, step and hexagon densities at the growing nanotube edge at three temperatures $T = 0.25; 1.0; 10.0$ for systems (42,6) (panels a, c, d) and (42,2) (panels b,d,e) obtained by KMC simulations. Some densities show oscillations that fade away with growth time.

state are proportional to the class number c. This means that moving of carbon adatoms to steps should be the growth rate-limiting process. More calculations are needed to substantiate this physical picture of the displayed results.

In Fig. 14, we report the time evolution of the number of steps, adatoms and hexagons at the CNT edge at different temperatures with $\Delta\mu = 0.25$. Oscillations are observed in some measured quantities. This results from the competition between growth and diffusion events in the early stage of the growth. Fig. 14a evidences a step propagation mode. Indeed, at $T = 0.25$ and $T = 1.0$ the number of steps $N_s(t)$ is close to $N_s(t = 0) = 6$. These numbers are almost constant during the growth. In Fig. 14b, $N_s(t)$ is higher than the initial number $N_s(t = 0) = 2$ in this temperature range. This means that other steps have been created on terraces by hexagons nucleation. On the contrary, at $T = 10.0$, $N_s(t)$ is not very far from $N_s(t = 0) = 2$ and a step propagation mode is expected since $N_h(t)$ is much lower than at $T = 0.25$ and $T = 1.0$.

5. Conclusion

A growth model is introduced to investigate the elongation rate of a chiral nanotube. The model comprises deposition, inlayer and interlayer diffusion events at the edge. A kinetic equation that describes the edge profile fluctuations is written and solved by means of exact and Monte Carlo methods. The elongation rate of the nanotube is extracted as function of model parameters which are the synthesis temperature, the pressure of the gaseous carbon phase, the chiral index of the nanotube and the growth time. Results achieved indicated that layer-by-layer growth is possible at the edge and an exact growth phase diagram has been devised for a finite-size system. Spiral growth by step propagation has been detected in the early stage of the growth process for some values of the parameters. The interlayer diffusion mechanism enhanced the growth rate at high temperature when the diffusion rate includes a temperature-dependent attempt frequency. In some parameters ranges, the edge relaxation by carbon atoms diffusion can also lead to unstable growth by completely faceting the nanotube edge. The achieved results have been compared to some reported in previous works and an agreement was obtained, in particular in the correlation between the growth rate and the carbon nanotube chirality.

Declaration of competing interest

The authors declare that they have no known competing financial interests or personal relationships that could have appeared to influence the work reported in this paper.

References

[1] R.H. Baughman, A.A. Zakhidov, W.A. de Heer, Carbon nanotubes—The route toward applications, Science 297 (2002) 787–792.
[2] M. Vahdani Moghaddam, P. Yaghoobi, G.A. Sawatzky, A. Nojeh, ACS Nano. 9 (2015) 4064.
[3] N. Perea-Lopez, B. Rebollo-Plata, J.A. Briones-Leon, A. Morelos-Gomez, D. Hernandez-Cruz, G.A. Hirata, et al., ACS Nano. 5 (2011) 5072.
[4] L.V. Titova, C.L. Pint, Q. Zhang, R.H. Hauge, J. Kono, F.A. Hegmann, Nano Lett. 15 (2015) 3267.
[5] X. He, N. Fujimura, J.M. Lloyd, K.J. Erickson, A.A. Talin, Q. Zhang, et al., Nano Lett. 14 (2014) 3953.
[6] J.H. Taphouse, O.N.L. Smith, S.R. Marder, B.A. Cola, Adv. Funct. Mater. 24 (2014) 465.
[7] S.M. Bachilo, L. Balzano, J.E. Herrera, F. Pompeo, D.E. Resasco, R.B. Weisman, J. Am. Chem. Soc. 125 (2003) 11186.
[8] S. Maruyama, Y. Miyauchi, Y. Murakami, S. Chiashi, New J. Phys. 5 (2003) 149.141–149.112.
[9] Y. Ando X. Zhao T. Suga, M. Kumar, Materialstoday 7 (2004) 22.
[10] F. Ding, A.R. Harutyunyan, B.I. Yakobson, Proc. Natl. Acad. Sci. USA 106 (2009) 2506, http://dx.doi.org/10.1073/pnas.0811946106.
[11] V.I. Artyukhov, E.S. Penev, B.I. Yakobson, Nature Commun. 5 (2014) 4892.
[12] M. He, et al., Sci. Adv. 5 (2019) eaav9668, http://dx.doi.org/10.1126/sciadv.aav9668.
[13] F. Zounmenou, R.D. Hontinfinde, F. Hontinfinde, Physica A 594 (2022) 127013.
[14] A.B. Bortz, M.H. Kalos, J.L. Lebowitz, J. Comput. Phys. 17 (1975) 10.
[15] A.V. Kpadonou, F. Hontinfinde, Physica A 362 (2006) 345.
[16] F. Hontinfinde, M. Touzani, Surf. Sci. 338 (1995) 236.
[17] F. Hontinfinde, R. Ferrando, A.C. Levi, Physica A 319 (2003) 36.
[18] F. Hontinfinde, J. de Phys. I 7 (1997) 767.
[19] R. Ferrando, F. Hontinfinde, A.C. Levi, Phys. Rev. B 56 (1997) 4406.
[20] U.T. Ndongmouo, F. Hontinfinde, Surf. Sci. 571 (2004) 89.
[21] S.I.V. Hontinfinde, A. Akpo, F. Hontinfinde, Eur. Phys. J. B 89 (2016) 215.
[22] F. Hontinfinde, J. Krug, M. Touzani, Physica A 237 (1997) 363.
[23] M. Kotrla, A.C. Levi, J. Stat. Phys. 64 (1991) 579.
[24] R.J. Glauber, J. Math. Phys. 4 (1963) 294.
[25] W. Lenz, Z. Phys. 21 (1920) 613.
[26] E. Ising, Z. Phys. 31 (1925) 253.
[27] J. Krug, F. Hontinfinde, J. Phys. A 30 (1997) 7739.
[28] R. Becker, W. Doering, Ann. Phys. (Leipzig) 24 (1935) 179.
[29] G.H. Gilmer, J. Cryst. Growth 42 (1977) 3.
[30] J.D. Weeks, G.H. Gilmer, Adv. Chem. Phys. 40 (1979) 157.
[31] A. Wilson, Phil. Mag. 50 (1900) 609.
[32] J. Frenkel, Phys. Z. Sowjetunion 1 (1932) 498.
[33] W.K. Burton, N. Cabrera, F.C. Frank, Nature 163 (1949) 398.
[34] F. Yang, X. Wang, D. Zhang, K. Qi, J. Yang, Z. Xu, M. Li, X. Zhao, X. Bai, Y. Li, J. Am. Chem. Soc. 137 (2015) 8688.
[35] M. He, Y. Magnin, H. Amara, H. Jiang, H. Cui, F. Fossard, A. Castan, E. Kauppinen, A. Loiseau, C. Bichara, Carbon 113 (2017) 231.